Multi-wavelength observations of IGR J17544-2619 from quiescence to outburst

E. Bozzo, V. Bhalerao, P. Pradhan, J. Tomsick, P. Romano, C. Ferrigno, S. Chaty, L. Oskinova, A. Manousakis, R. Walter, et al.

A&A 596, A16 (2016)
DOI: 10.1051/0004-6361/201629311

Astronomy & Astrophysics

Multi-wavelength observations of IGR J17544-2619 from quiescence to outburst

E. Bozzo[1], V. Bhalerao[2], P. Pradhan[3,4], J. Tomsick[5], P. Romano[6], C. Ferrigno[1], S. Chaty[7,8], L. Oskinova[9], A. Manousakis[10], R. Walter[1], M. Falanga[11,12], S. Campana[13], L. Stella[14], M. Ramolla[15], and R. Chini[15,16]

[1] ISDC Data Centre for Astrophysics, Chemin d'Ecogia 16, 1290 Versoix, Switzerland
e-mail: enrico.bozzo@unige.ch
[2] Inter-University Center for Astronomy and Astrophysics, Post Bag 4, Ganeshkhind, 411007 Pune, India
[3] St. Josephs College, Singamari, 734104 Darjeeling, West Bengal, India
[4] North Bengal University, Raja Rammohanpur, 734013 District Darjeeling, West Bengal, India
[5] Space Sciences Laboratory, 7 Gauss Way, University of California, Berkeley, CA 94720-7450, USA
[6] INAF, Istituto di Astrofisica Spaziale e Fisica Cosmica – Palermo, via U. La Malfa 153, 90146 Palermo, Italy
[7] Laboratoire AIM, UMR 7158, CEA/DRF/Irfu/SAp-CNRS-Université Paris Diderot, Centre de Saclay, L'Orme des Merisiers, Bât. 709, 91191 Gif-sur-Yvette Cedex, France
[8] Institut Universitaire de France, 103 boulevard Saint-Michel, 75005 Paris, France
[9] Institut für Physik und Astronomie, Universität Potsdam, Karl-Liebknecht-Str. 24/25, 14476 Potsdam, Germany
[10] Centrum Astronomiczne im. M. Kopernika, Bartycka 18, 00-716 Warszawa, Poland
[11] International Space Science Institute (ISSI), Hallerstrasse 6, 3012 Bern, Switzerland
[12] International Space Science Institute in Beijing, No. 1 Nan Er Tiao, Zhong Guan Cun, Beijing 100190, PR China
[13] INAF – Osservatorio Astronomico di Brera, via Emilio Bianchi 46, 23807 Merate (LC), Italy
[14] INAF – Osservatorio Astronomico di Roma, via Frascati 33, 00044 Rome, Italy
[15] Ruhr-Universität Bochum, 44780 Bochum, Germany
[16] Instituto de Astronomía, Universidad Católica del Norte, Avenida Angamos 0610, Antofagasta, Chile

Received 14 July 2016 / Accepted 9 October 2016

ABSTRACT

In this paper we report on a long multi-wavelength observational campaign of the supergiant fast X-ray transient prototype IGR J17544-2619. A 150 ks-long observation was carried out simultaneously with *XMM-Newton* and *NuSTAR*, catching the source in an initial faint X-ray state and then undergoing a bright X-ray outburst lasting approximately 7 ks. We studied the spectral variability during outburst and quiescence by using a thermal and bulk Comptonization model that is typically adopted to describe the X-ray spectral energy distribution of young pulsars in high mass X-ray binaries. Although the statistics of the collected X-ray data were relatively high, we could neither confirm the presence of a cyclotron line in the broad-band spectrum of the source (0.5−40 keV), nor detect any of the previously reported tentative detections of the source spin period. The monitoring carried out with *Swift*/XRT during the same orbit of the system observed by *XMM-Newton* and *NuSTAR* revealed that the source remained in a low emission state for most of the time, in agreement with the known property of all supergiant fast X-ray transients being significantly sub-luminous compared to other supergiant X-ray binaries. Optical and infrared observations were carried out for a total of a few thousand seconds during the quiescence state of the source detected by *XMM-Newton* and *NuSTAR*. The measured optical and infrared magnitudes were slightly lower than previous values reported in the literature, but compatible with the known micro-variability of supergiant stars. UV observations obtained with the UVOT telescope on-board *Swift* did not reveal significant changes in the magnitude of the source in this energy domain compared to previously reported values.

Key words. X-rays: binaries

1. Introduction

Supergiant Fast X-ray Transients (SFXTs) are a subclass of supergiant high-mass X-ray binaries (SgXBs) mostly known for their peculiarly short X-ray outbursts, lasting a few hours at the most, and the much reduced average X-ray luminosity compared to the so-called classical SgXBs (see, e.g., Walter et al. 2015, for a recent review). In both classical SgXBs and SFXTs, the bulk of the X-ray emission is due to the accretion of the supergiant star wind onto a compact object, typically a neutron star (NS). The origin of the extreme X-ray variability of the SFXTs is still not well understood, but it is generally believed that the short outbursts are triggered by the presence of dense clumps in the stellar wind surrounding the NS (in't Zand 2005; Walter & Zurita Heras 2007; Negueruela et al. 2006; Oskinova et al. 2012; Bozzo et al. 2016), while the reduction in the average luminosity can be ascribed to different mechanisms that inhibit the accretion for a large fraction of the time. The proposed mechanisms comprise either a magnetic and/or centrifugal gating (Grebenev & Sunyaev 2007; Bozzo et al. 2008), or the onset of a quasi-spherical settling accretion regime (Davies & Pringle 1981; Shakura et al. 2012).

IGR J17544-2619 is the prototype of the SFXTs and was discovered in 2003 with INTEGRAL during a 2 h long flare (Sunyaev et al. 2003). Since then, the source has been showing the most extreme X-ray variability among all other objects of the same class. It is characterized by an orbital period of 4.9 days (Clark et al. 2009), one of the shortest measured among the SFXTs, and a quiescent X-ray luminosity that can be as several times $\sim 10^{32}$ erg s^{-1}(in't Zand 2005). Bright outbursts from IGR J17544-2619 were observed on many occasions by

different instruments (see, e.g., Sguera et al. 2006; Rampy et al. 2009; Romano et al. 2011, and references therein). So far, the most luminous event was caught by *Swift* in 2014 reaching approximately 3×10^{38} erg s^{-1} in the 0.5−10 keV energy range (assuming a source distance of 3.5 kpc; Pellizza et al. 2006; Rahoui et al. 2008). In the paper reporting the discovery of such intense X-ray emission (Romano et al. 2015), the authors suggested that a temporary accretion disk could have formed around the NS, as the high luminosity recorded is virtually impossible to be reached in a wind-fed system. In the same paper, evidence of a possible pulsation at 11.6 s was reported, but never confirmed (as well as the previous hint at 71 s; Drave et al. 2012). A likely cyclotron line at 17 keV has been discovered in a *NuSTAR* observation carried out in 2013 (Bhalerao et al. 2015), making IGR J17544-2619 the first SFXT for which a direct measurement of the magnetic field is available ($B \simeq 1.5 \times 10^{12}$ G). The properties of the supergiant companion hosted in IGR J17544-2619 were recently investigated in depth by Giménez-García et al. (2016), confirming it to be a O9I supergiant.

In this paper, we report on a 150 ks-long observational campaign performed in the direction of IGR J17544-2619 using *XMM-Newton* and *NuSTAR* simultaneously. During these observations, the source remained in a very low quiescent state for most of the time, and then, toward the end of the observations, it underwent a bright outburst comprising three distinct short flares lasting in total approximately 7 ks. We took advantage of the high statistics and good energy resolution of the instruments onboard *XMM-Newton* and *NuSTAR* to investigate the properties of the source's X-ray emission during the quiescence and outburst periods. We also report on the results of the *Swift*/XRT monitoring performed for approximately one week around the time of the *XMM-Newton* and *NuSTAR* observations and covering more than one orbital revolution of the system. We summarize the data analysis techniques in Sect. 2 and present the results in Sects. 3 and 4. The results of several optical and infrared observations carried out during the source quiescent period caught by *XMM-Newton* and *NuSTAR* are summarized in Sect. 5. Our discussion and conclusions are provided in Sect. 6.

2. X-ray data analysis

2.1. XMM-Newton

The *XMM-Newton* observation of IGR J17544-2619 began on 2015-03-20 05:00:31 UT and lasted until 2015-03-21 20:17:09 UT (OBSID: 0744600101; PI: E. Bozzo), resulting in a total exposure time of ∼141 ks (i.e., approximately 30% of the source orbital period). The EPIC-pn and MOS1 cameras were operated in full frame, while the MOS2 was in timing mode. Data were also collected with the two grating instruments RGS1 and RGS2. All observation data files (ODFs) were processed using the *XMM-Newton* Science Analysis System (SAS 15.0) following standard procedures[1]. The observation was heavily affected by a flaring background during the first ∼120 ks. Removing the high background time interval resulted in an effective exposure time of approximately 60 ks for all the EPIC cameras and the two RGSs. The regions used for the extraction of the source spectra and lightcurves were chosen for all instruments to be centered on the best known position of IGR J17544-2619, as reported by in't Zand (2005). The source displayed a large variability in X-rays (more than three orders of magnitudes, see

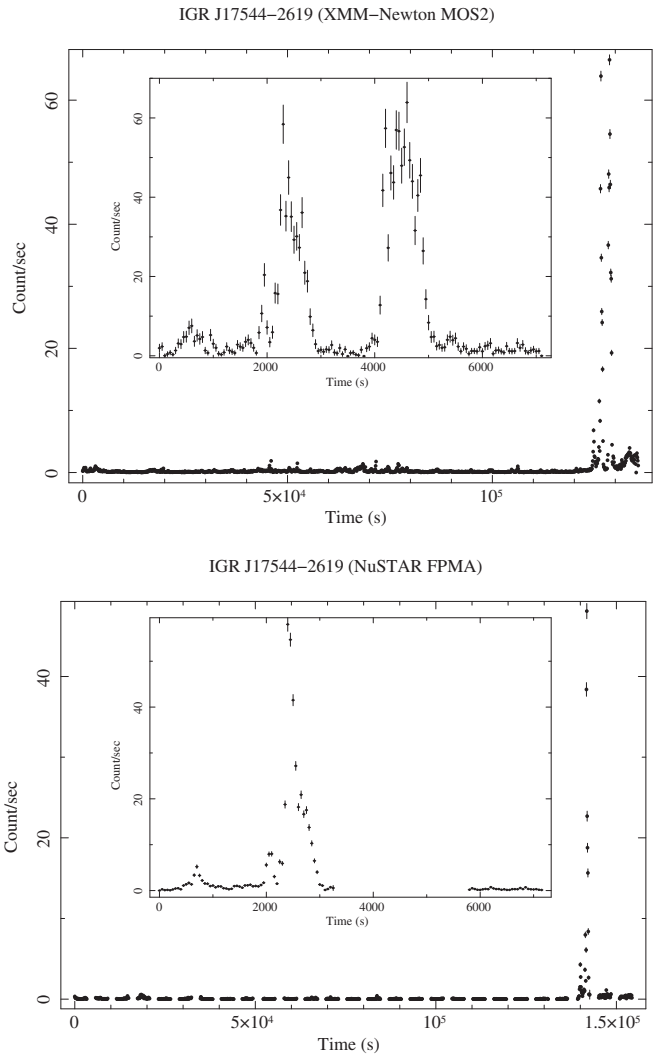

Fig. 1. *Top*: *XMM-Newton* MOS2 lightcurve of IGR J17544-2619 in the 0.5−10 keV energy band. The lightcurve has not been filtered for the high flaring background time intervals. The *insert* shows a zoom in the outburst of the source occurring towards the end of the observation and comprised of three distinct flares. The time bin of the main lightcurve is 100 s, while for the lightcurve in the insert we used a time bin of 50 s. The start time of the main lightcurve is 2015 March 20 at 06:02:34 UTC (57 101.2518 MJD), while the start time of the zoomed lightcurve in the insert is 2015 March 21 at 15:48:44 UTC (57 102.6588 MJD). *Bottom*: *NuSTAR* FPMA lightcurve in the 5−10 keV energy band. The time bin is 100 s and the start time is 2015 March 20 at 1:06 UTC (57 101.0458 MJD). The *inset* shows a zoom into the flaring part of the *NuSTAR* lightcurve (in this case the start and the bin times are the same as those of the *inset in the top figure*).

Fig. 1), and thus the size and shape of the extraction regions for all instruments had to be carefully changed for different time intervals.

We used a circular region during periods in which the source count-rate was $\lesssim$0.5 cts s^{-1} for the MOS1 and $\lesssim$2.0 cts s^{-1} for the pn[2]. At higher count-rates, an annular region was used to avoid pile-up issues. The size of the inner hole of the annuls was changed from 50 to 450 pixels depending on the brightness of the source. The external radius of both the circular and annular region was also varied with this source intensity, ranging from 650 pixels during the quiescent period to 1000 pixels

[1] http://www.cosmos.esa.int/web/xmm-newton/sas-threads

[2] https://heasarc.gsfc.nasa.gov/docs/xmm/uhb/epicmode.html

during the brightest part of the flares. For each pn and MOS1 spectra in which the correction for pile-up was needed, the removal of such effects was verified by comparing the results of the spectral fits with the MOS2 data. The latter, being in timing mode, was not affected by pile-up even during the peak of the flares (we cross-checked this finding by using the SAS EPAPLOT task). The background spectra and lightcurves were extracted for all EPIC cameras by using regions close to the position of IGR J17544-2619 but not contaminated by the source emission. All lightcurves were corrected for any remaining instrumental effect (e.g., vignetting) by using the EPICLCCORR task. Throughout this publication we indicate uncertainties on all quantities at 90% confidence level, unless stated otherwise.

We show the MOS2 lightcurve of the source in the 0.5−10 kev energy range in Fig. 1, as this one is not affected by pile-up. As anticipated in Sect. 1, the source remained in a low emission state for the initial 120 ks of the observation and then underwent a 7 ks long outburst, comprising three fast flares occurring approximately during the periastron passage (see details in Sect. 6). The first flare was much fainter than the following two (by a factor of 10−20). The average 0.5−10 keV count-rate of the source during the quiescent period in the MOS2 was of 0.090 ± 0.001 cts s^{-1}, while the peak count-rate registered during one of the three flares achieved 82 ± 12 cts s^{-1} when the lightcurve was binned at 10 s. In Fig. 2 we also show the hardness ratio (HR) of two MOS2 lightcurves extracted in the 0.5−2.5 keV and 2.5−10 keV energy bands. An adaptive rebinning has been used, following the same technique adopted in a number of our previous papers (see, e.g., Bozzo et al. 2013), to achieve a minimum signal-to-noise ratio (S/N) of 15 at each point.

Evidence for coherent and quasi-coherent oscillations in the *XMM-Newton* data were searched for using event files from the source where the arrival times of all photons were barycentre-corrected. No significant detection could be found in the all accessible frequency range (∼10^{-5}−300 Hz).

2.2. NuSTAR *data*

IGR J17544–2619 was observed by *NuSTAR* from 2015 March 20 at 00:51:07 to March 21 at 20:01:07 (UTC; PI: Bhalerao). The Target of Opportunity observation (OBSID 90001005002; PI: Bhalerao) was triggered in order to obtain as much simultaneous data as possible with the scheduled *XMM-Newton* observation (see Sect. 2.1). After having applied all the good time intervals (GTI) to the *NuSTAR* data accounting for the Earth occultation and the South Atlantic Anomaly passages, we obtained an effective exposure time of 61.3 ks and 62.8 ks for the Focal Plane Modules A and B, respectively. The data were processed using Nustardas v1.5.1, and CALDB dated 2015 September 4. The source photons were extracted from a 60 arcsec circle centred on the source, while the background was evaluated using polygonal extraction regions on the same chip. In NuSTAR FPMB, the source region was contaminated by stray light. We selected a background region with the same level of contamination to ensure that this stray light did not affect our results. The average source count-rate recorded for most of the observation was approximately 0.1−0.2 cts s^{-1} (3−80 keV energy band), yielding nearly 100% live time. During the source outburst at the end of the observation, a count-rate as high as ∼50 counts/s was measured.

We show in Fig. 1 the entire *NuSTAR* lightcurve of IGR J17544-2619 as observed by the FPMA in the 5−10 keV energy band, while in Fig. 2 we report a zoom in the *NuSTAR*

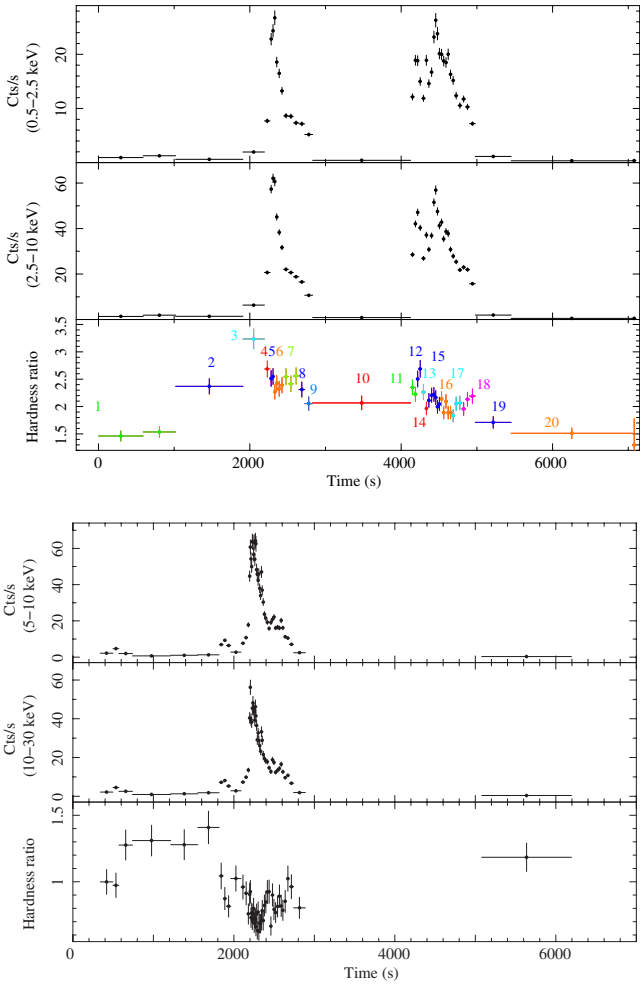

Fig. 2. Lightcurves in different energy bands and the corresponding hardness ratio obtained from the flaring part of the *XMM-Newton* (*top*) and *NuSTAR* (*bottom*) observations. In both cases an adaptive rebinning has been used to achieve $S/N \gtrsim 15$ in each bin. We do not show the quiescent portion of the lightcurve, as there, the statistics were much lower than during flares and thus no meaningful HR resolved spectral analysis could be carried out. Here the start time of the *NuSTAR* and *XMM-Newton* lightcurves are the same. The third flare could not be detected by *NuSTAR* due to visibility constraints. In the *top* figure, we highlighted the 20 intervals in which the HR-resolved spectra analyzed in Sect. 3 have been extracted with different colors.

lightcurves extracted in the 3−10 keV and 10−30 keV, together with the corresponding HR. In this plot, an adaptive rebinning has been used to achieve $S/N \gtrsim 15$ in each time bin as for the *XMM-Newton* case (see Sect. 2.1). *NuSTAR* observed only two of the three flares displayed by the source during the outburst. The third flare could not be observed due to the satellite visibility constraints.

Due to the lack of any significant detection in the *XMM-Newton* data (see Sect. 2.1) and the known issues affecting X-ray timing analyses with *NuSTAR* (see Bachetti et al. 2015, and references therein), we did not perform detailed searches for coherent and quasi-coherent modulations of the events recorded by the FPMA and FPMB.

2.3. Swift *data*

IGR J17544-2619 was observed by *Swift* as a ToO campaign (PI: Romano) aimed at monitoring the general flux level of

Table 1. Log of all *Swift*/XRT observations used in the present paper.

Sequence	Obs/mode	Start time (MJD)	End time (MJD)	Exposure (s)
00035056169	XRT/PC	57 099.2711	57 099.4715	3395
00035056170	XRT/PC	57 100.6156	57 100.8097	3896
00035056171	XRT/PC	57 101.0023	57 101.2735	878
00033707001	XRT/PC	57 101.0038	57 101.2853	3962
00033707002	XRT/PC	57 101.1454	57 101.1569	980
00035056173	XRT/PC	57 102.0620	57 102.2798	4874
00035056174	XRT/PC	57 103.5947	57 103.8041	4969
00035056175	XRT/PC	57 104.5921	57 104.7381	2841
00035056176	XRT/PC	57 107.7829	57 107.8582	2061

the source around the *XMM-Newton* observation, with six daily observations, each 5 ks long, starting on 2015 March 18. As the orbital period of the source is approximately 4.9 days (see Sect. 1), the XRT (Tueller et al. 2005) and UVOT (Roming et al. 2005) data covered slightly more than an entire orbital revolution of IGR J17544-2619. The complete log of the XRT observations is provided in Table 1, while for UVOT we summarize all relevant information in Table 2.

The XRT data were processed and analyzed using the standard software (FTOOLS v6.16), calibration files (CALDB 20140709), and methods. All data were processed and filtered with XRTPIPELINE (v0.13.1). The source remained at a level of a few $\times 10^{-2}$ counts s^{-1} throughout the campaign, and only flared up to 0.17 cts s^{-1} on March 22 (obs. 00035156174). As the source was never affected by pile-up, all events were accumulated within a circular region with a radius of 20 pixels (where 1 pixel corresponds to $\sim$2.″36), while background events were accumulated from an annular source-free region with inner/outer radii of 70/100 pixels centered on the source. When no detection was achieved in one observation, we calculated the corresponding 3σ upper limit by using the SOSTA and UPLIMIT tools available within XIMAGE, together with the Bayesian method for low count experiments (Kraft et al. 1991). The XRT lightcurves were corrected for point spread function losses, vignetting, and were background subtracted.

The XRT data showed that the source remained in a relatively low X-ray emission state during the entire monitoring campaign. Only a short flare was recorded, reaching approximately 0.17 cts s^{-1} in the energy band of the instrument. Excluding this flare, the average count-rate recorded by XRT from the source was approximately 0.025 ± 0.003 cts s^{-1} in the 0.5–10 keV energy range. This corresponds to a flux of 2.7×10^{-12} erg cm^{-2} s^{-1} when an absorbed power-law model with $N_{\rm H} = 2 \times 10^{22}$ cm^{-2} and $\Gamma = 1$ is used for the conversion (see Sect. 3). Due to the relatively low statistics of the XRT observations, no useful timing and spectral analysis of these data could be carried out.

UVOT observed IGR J17544-2619 simultaneously with the XRT using different filters (B, $M2$, U, V, $W1$, and $W2$) in different observations in order to provide the broadest wavelength coverage possible. The data analysis was performed using the UVOTIMSUM and UVOTSOURCE tasks included in the FTOOLS software. The latter task calculates the magnitude through aperture photometry within a circular region and applies specific corrections due to the detector characteristics. We provide a summary of all results in Table 2, where the magnitudes have been computed for each filter by combining data with the same filter in different observations. The reported magnitudes are on the UVOT photometric system described in Breeveld et al. (2011) and are not corrected for Galactic extinction. We did not find significant differences in the estimated magnitudes of the source in all filters compared to values obtained during previous monitoring campaigns (and compatible with expected values for the supergiant star hosted in IGR J17544-2619; Romano et al. 2011).

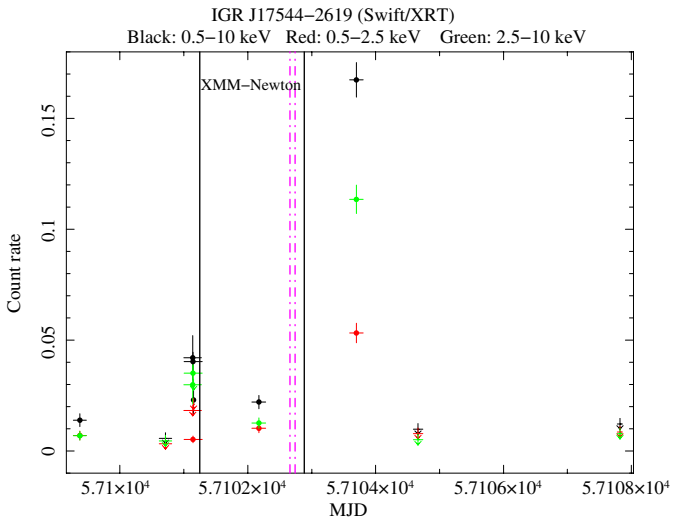

Fig. 3. Lightcurves obtained from the *Swift*/XRT monitoring campaign performed a few days before and after the *XMM-Newton* and *NuSTAR* observations of IGR J17544-2619 (we mark in black the lightcurve in the 0.5–10 keV energy range, in red the lightcurve in the 0.5–2.5 keV energy range, and in green the lightcurve in the 2.5–10 keV energy range). The time is measured from the 57 102 MJD, as in Fig. 1. The faint flare recorded by XRT, which is visible above when the source count-rate reaches approximately 0.17 cts s^{-1}, occurred on 57 103.7 MJD, that is, roughly one day after the onset of the much brighter outburst observed by *XMM-Newton* and *NuSTAR*. The downward arrows indicate 3σ upper limits on the source count-rate when IGR J17544-2619 was not detected in the corresponding XRT observation. We also marked with vertical solid lines the time interval of the *XMM-Newton* observation (the *NuSTAR* observation is nearly simultaneous). The vertical, dashed magenta lines indicate the time interval of the 7 ks outburst detected by *XMM-Newton* and *NuSTAR* (see Sects. 2.1 and 2.2).

Table 2. Summary of UVOT results.

MJD[a]	Filter	Magnitude
$57\,103.5639 \pm 4.2257$	B	14.53 ± 0.03
$57\,104.2429 \pm 3.5599$	$M2$	20.29 ± 0.15
$57\,103.5623 \pm 4.2256$	U	15.19 ± 0.03
$57\,104.2397 \pm 3.5582$	V	12.81 ± 0.02
$57\,103.5647 \pm 4.2936$	$W1$	16.63 ± 0.04
$57\,103.5680 \pm 4.2281$	$W2$	17.92 ± 0.05

Notes. The indicated uncertainties on the observational times correspond to the time coverage of the combined images obtained with the same filter in different observations.

3. Spectral analysis with phenomenological models

We first extracted the *XMM-Newton* and *NuSTAR* spectra averaged during the entire observation and only during the quiescent period. When averaged over the entire observation, both the MOS1 and the pn data were heavily piled-up and the comparison with the MOS2 data revealed that it was not possible to find a satisfactorily correction for this issue to obtain compatible results for all cameras simultaneously. For this reason, we only

used the MOS2, RGS, and *NuSTAR* data to analyze the properties of the source X-ray emission averaged over the entire available exposure time. During quiescence, the source emission was too faint to obtain meaningful RGS spectra, and thus we did not include the corresponding data in the combined *XMM-Newton* and *NuSTAR* fit.

We adopted several different phenomenological models to describe the broad-band spectra of IGR J17544-2619. Due to the complex spectral energy distribution in the 0.5−40 keV energy range (see, e.g., Figs. 4 and 7), we could only achieve acceptable results by using a combination of an absorbed thermal blackbody (BBODYRAD in XSPEC) plus a power-law with a high-energy cut-off (HIGHECUT*POW in XSPEC). This model has often been used to describe the X-ray emission of highly magnetized accreting pulsars (see, e.g., White et al. 1995; Coburn et al. 2001). The thermal component is most likely originating from the NS surface, while the power-law might originate from Comptonization within its accretion column or other non-thermal processes. A weak iron K_α line at 6.4 keV was detected in the spectra averaged over the entire observational period. This is likely produced by fluorescence due to the X-ray illumination of the stellar wind material surrounding the compact object hosted in IGR J17544-2619, as the measured equivalent width is relatively small and comparable to that observed in a large number of wind-fed HMXBs (see, e.g., Bozzo et al. 2008; Torrejón et al. 2010; Manousakis & Walter 2011; Giménez-García et al. 2015, and references therein). We summarize all results obtained with the phenomenological model in Table 3 and show in Fig. 4 the unfolded combined *XMM-Newton* + *NuSTAR* spectra corresponding to the entire observation and the quiescent period only.

In order to study possible spectral variations that could give rise to the changes in the HR visible in Fig. 2, we carried out a hardness ratio resolved spectral analysis of the outburst period. We did not carry out the same analysis during the quiescent period due to the much-reduced statistics of the data. We selected 20 different intervals, as shown in the upper panels of Fig. 2 and fit all of them with the same two-component model described above. As the third flare was not observed by *NuSTAR* due to the satellite visibility constraints, no high-energy coverage (>10 keV) was available for the spectra extracted during the time intervals 11−19. These time intervals are thus not included among all the broad-band results presented in Table 3.

From the values reported in the table we found that there was a significant increase in the absorption column density local to the source immediately before the rise to the second flare in the outburst (the first one was too faint to reveal any significant spectral variability). The $N_{\rm H}$ dropped by a factor of ∼1.5 when the source reached the peak of the flare and then remained virtually constant throughout the rest of the observation. The thermal component is observed to increase in temperature and in radius toward higher fluxes, where the Comptonization component clearly becomes dominant. In order to visually show these variations, we report in Fig. 7 the case of the spectra extracted during the time interval 6, close to the peak of the second flare, and the time interval 9, half way through the decay from this flare.

A puzzling result is found during the time interval 10, which corresponds to the low count-rate period separating the second and the third flare. The spectra extracted during this interval (only partially covered by *NuSTAR*) are shown in Fig. 5. As the source flux in this interval dropped significantly, the pn spectrum was not affected by pile-up. An evident absorption feature is detected at 7.2 keV. By adding a Gaussian absorption component to the spectrum, we measured a centroid energy of 7.21 ± 0.14 keV and a width of 0.2 ± 0.1 keV (the latter being compatible with a broadening due to the limited energy resolution of the pn). The estimated equivalent width of the line and the associated uncertainty is $0.23^{+0.11}_{-0.06}$ keV, thus suggesting a detection significance $>3\sigma$. Adding the line to the fit of all spectra in the interval 10 (i.e., the combined fits of MOS1, MOS2, pn, FPMA, and FPMB) leads to a decrease of the $\chi^2_{\rm red}$ from $\chi^2_{\rm red}$/d.o.f. = 0.93/214 (fit without the line) to $\chi^2_{\rm red}$/d.o.f. = 0.86/211 (fit with the line included). This again suggests a detection significance at the level of $\gtrsim 3\sigma$ according to the F-test included within XSPEC.

The lack of *NuSTAR* data for the time intervals 11−19 prevented an analysis of the remaining time-resolved spectra comparable to that discussed above. For each interval, the *XMM-Newton* data alone could be reasonably well-fitted by

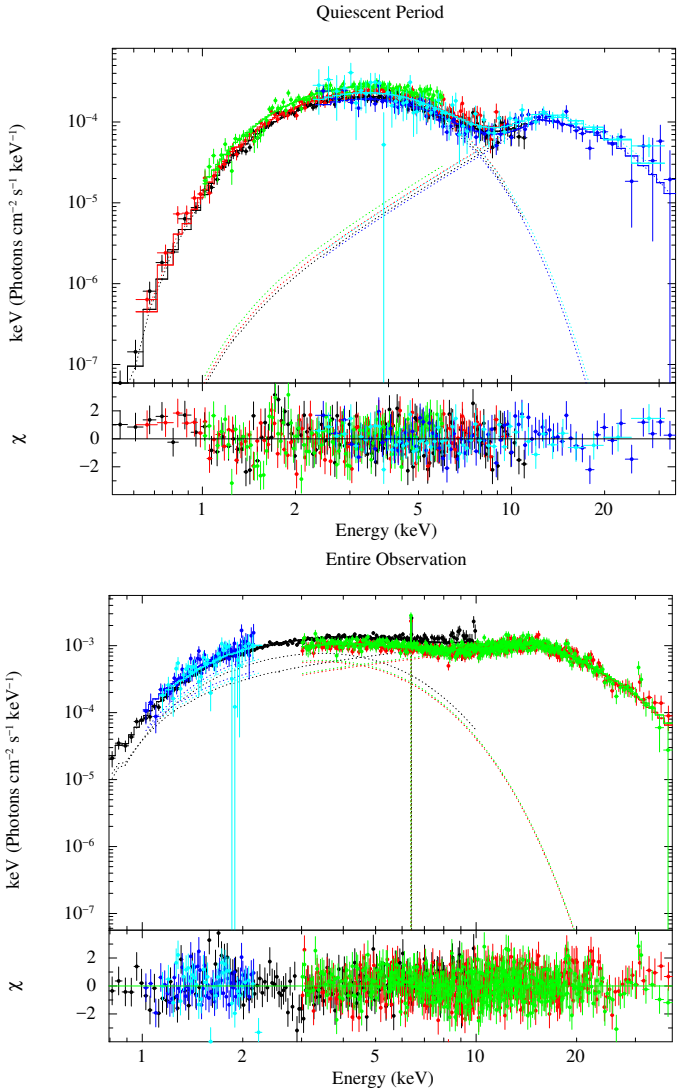

Fig. 4. *Top*: combined *XMM-Newton* and *NuSTAR* unfolded spectra extracted during the first ∼120 ks of the observations, when the source was in a quiescent state. The EPIC-pn is in black, the MOS2 in red, the MOS1 in green, the FPMA in blue, and the FPMB in cyan. The best fit model is obtained by using a combination of an absorbed blackbody plus a power-law with a high energy cut-off (see Sect. 3 for details). The residuals from the best fit are shown in the bottom panel. *Bottom*: same as above but for the spectra accumulated during the entire observational period. The MOS2 is in black, the FPMA in red, the FPMB in green, the RGS1 in blue, and the RGS2 in cyan. The same model as above plus a weak iron emission line at ∼6.4 keV, has been used to obtain the best fit. Residuals from this fit are shown in the *bottom panel*.

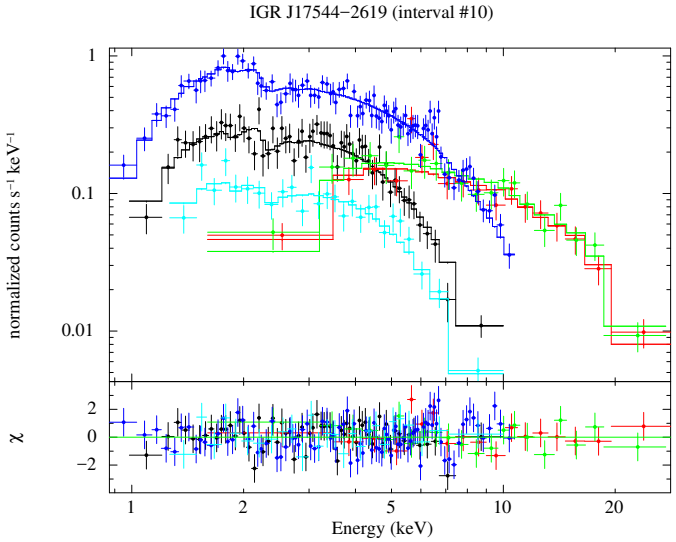

Fig. 5. *XMM-Newton* and *NuSTAR* spectra extracted during the time interval 10. This is the only interval in which a spectral feature is observed around ∼7.2 keV. The best fit model to describe the continuum in this case is the same mentioned in Fig. 7. The residuals from the best fit are shown in the bottom panel and no component was added to take the presence of the feature into account in order to highlight its significance.

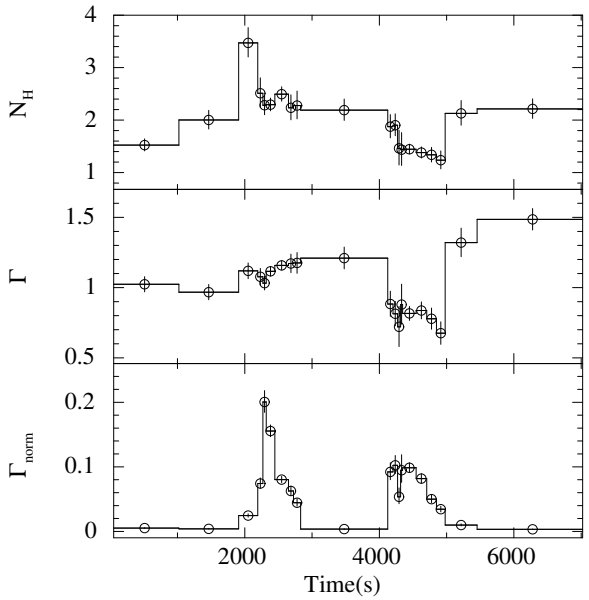

Fig. 6. Results obtained when the time-resolved *XMM-Newton* data alone are fitted with a simple absorbed power-law model. *From the top to the bottom panel* we show the absorption column density, the power-law photon index, and its normalization. As discussed in the text, it is evident that the most prominent spectral changes took place during the second flare (the first one being much fainter than the other two and occurring in this figure at approximately t = 500 s). The uncertainties on the x axis correspond to the integration times of the spectra 1−20 in Fig. 2.

using a simple, absorbed power-law model. We verified that using the two-component models considered above for the broad-band spectral fits on the time-resolved *XMM-Newton* spectra alone always resulted in very poorly constrained parameters. In order to have a complete overview of the time-resolved spectral analysis achievable with *XMM-Newton*, we thus report in Fig. 6 a plot of all spectral parameters obtained by fitting the *XMM-Newton* data (MOS2 plus MOS1 and pn, when available) in the time intervals 1−20 with a simple absorbed power-law model. From this plot, it is evident that most of the spectral changes occurred during the second flare, while for the third flare only minor variations in the absorption column density and power-law photon index were measured. We were thus lucky to have the second flare, rather than the third one, observed simultaneously with *NuSTAR*.

We note that in neither the time-resolved nor the averaged spectra could we find a clear indication for the presence of the cyclotron line at ∼17 keV reported previously by Bhalerao et al. (2015). If a cyclotron line is added to the phenomenological model used in this section to fit the broad-band spectra of IGR J17544-2619, the centroid energy of this feature is moved by XSPEC approximately 8 keV and its width becomes as large as 2−3 keV. We did not consider this a reasonable model because a feature at 8 keV could not be the fundamental energy of the previously detected cyclotron lines from the source at 17 and 33 keV, and, additionally, the feature was evidently used by the XSPEC fitting routine to describe the "valley" in the energy range 6−9 keV where the soft and hard spectral components intersect one another. We thus do not discuss this model further. For completeness, instead, we tried to fit the two component model used in the present paper to the combined *Swift*/XRT and *NuSTAR* data reported previously by Bhalerao et al. (2015), where the cyclotron line was discovered. We used for the fit the same spectra extracted by these authors, as the latters are also among the collaborators of the present publication.

A fully reasonable fit was obtained with $\chi^2_{\rm red}$/d.o.f. = 0.85/144, $N_{\rm H}$ = 1.0 ± 0.3 cm^{-2}, $kT_{\rm BB}$ = 1.07 ± 0.04 keV, $E_{\rm cut}$ = $6.7^{+0.9}_{-6.7}$ keV, and $E_{\rm fold}$ = 4.6 ± 0.1 keV (we had to fix $\Gamma = -2.5$ in the fit as this parameter could not be constrained and the fit favored a largely negative power-law photon index). The presence of the cyclotron line remained clearly evident even from the residuals obtained with this model and we measured a centroid energy of 16.9 ± 0.5 keV, a depth of 0.5 ± 0.1 keV, and a 0.5−50 keV X-ray flux of 3.5×10^{-11} erg cm^{-2} s^{-1} in agreement with previous findings (Bhalerao et al. 2015). We thus concluded that, although we could not confirm the presence of the cyclotron line in IGR J17544-2619 with the newly obtained, strictly simultaneous *XMM-Newton* and *NuSTAR* observations, this feature did not disappear from the previous data-set when a different spectral model was used for the fit (note that the average flux of the source in the past and present observations is virtually the same).

4. Spectral analysis with a physical model

As SFXTs are believed to host young, highly magnetized accreting NSs and the spectral analysis above showed the presence of both a thermal and a non-thermal component in the spectrum of IGR J17544-2619, we also attempted a description of the X-ray emission from this object with a more physical model. In particular, we adopted the bulk and thermal Comptonization model (BW) described in detail by Ferrigno et al. (2009). The model is based on the original calculation of Becker & Wolff (2007), who computed the X-ray emission emerging from a cylindrical accretion column, typical of NS hosted in young high-mass X-ray binaries (and thus also in SgXBs). The model computes the bulk and thermal Comptonization of the seed photons that are produced by the bremsstrahlung, cyclotron, and

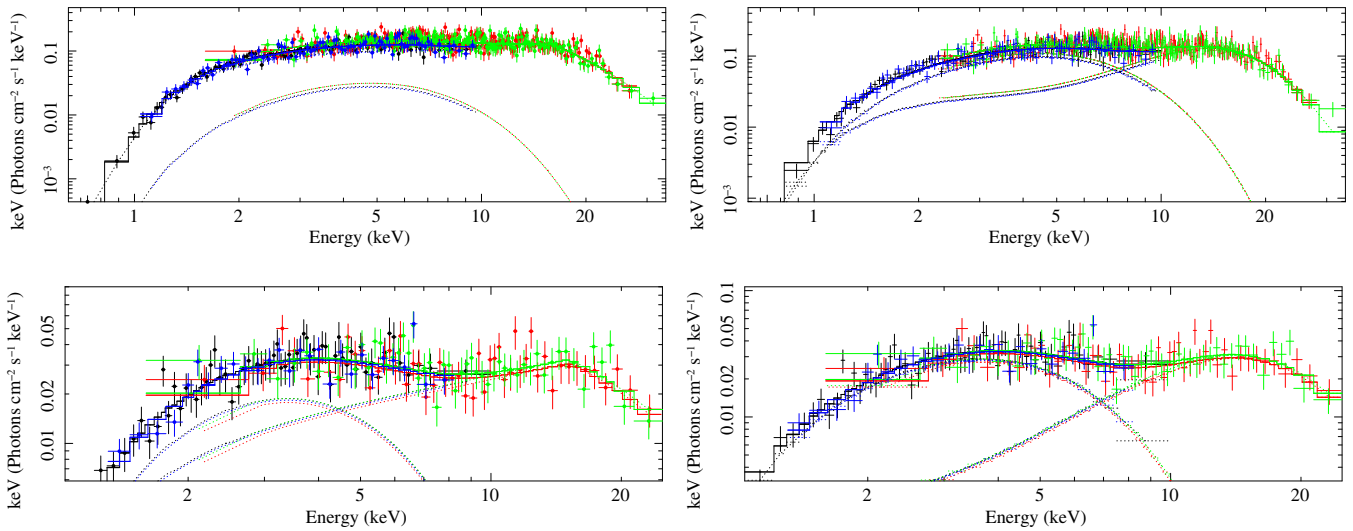

Fig. 7. An example of combined *XMM-Newton* and *NuSTAR* spectra during the decay from the second flare, as indicated in Fig. 2. We chose the spectra from the time interval 6 (*top panel*) and 9 (*bottom panel*) as examples to show how the source X-ray spectral emission evolves during the flare. For the figures on the *left*, the non-thermal component is described through the usage of a phenomenological HIGHECUT*POW model in XSPEC. For the panel on the *right*, the non-thermal component is fit by using the physical BW model (see Sect. 4). In both cases, it is evident that the non-thermal component dominates the source high-energy emission at higher fluxes (e.g., during the time interval used to extract the spectrum 6). The thermal component provides an increasingly important contribution to the overall emission during the decay from the flare (e.g., during the time interval used to extract the spectrum 9). The relative contribution of the thermal and non-thermal components is different in the fits performed with the phenomenological and physical spectral models, but the overall picture used to interpret the spectral change is qualitatively similar.

Table 3. Results of the fits to the combined *XMM-Newton* and *NuSTAR* spectra extracted in the time resolved intervals with the phenomenological model.

Parameter	All[a]	Quiescent	1	2	3	4	5	6	7	8	9	10[b]	20
$N_{\rm H}$	0.8 ± 0.06	1.14 ± 0.06	1.8 ± 0.3	0.96 ± 0.15	1.8 ± 0.3	1.1 ± 0.4	1.6 ± 0.3	1.8 ± 0.2	1.7 ± 0.2	1.2 ± 0.5	$1.3^{+0.6}_{-0.4}$	1.4 ± 0.3	1.2 ± 0.2
$kT_{\rm BB}$	$1.11^{+0.03}_{-0.01}$	1.08 ± 0.03	0.53 ± 0.01	1.37 ± 0.08	1.3 ± 0.1	1.35 ± 0.14	$1.7^{+0.5}_{-0.3}$	1.6 ± 0.2	$1.4^{+0.2}_{-0.1}$	1.1 ± 0.2	$1.1^{+0.2}_{-0.1}$	1.04 ± 0.1	0.90 ± 0.07
$N_{\rm BB}$	0.41 ± 0.03	0.12 ± 0.01	$12.6^{+18.1}_{-6.7}$	1.1 ± 0.2	$4.8^{+1.0}_{-0.8}$	$9.9^{+4.0}_{-5.0}$	$6.8^{+8.4}_{-4.2}$	$4.8^{+3.8}_{-2.6}$	$4.2^{+2.9}_{-2.4}$	12.0 ± 5.5	11.1 ± 4.7	0.7 ± 0.4	1.4 ± 0.3
Γ	0.42 ± 0.09	$-1.3^{+0.5}_{-0.8}$	0.7 ± 0.1	$-1.7^{+0.6}_{-0.7}$	$-0.13^{+0.3}_{-0.4}$	$0.3^{+0.4}_{-1.2}$	$0.8^{+0.1}_{-0.2}$	$0.92^{+0.09}_{-0.10}$	0.8 ± 0.1	$0.6^{+0.3}_{-0.5}$	$0.5^{+0.5}_{-1.5}$	$0.7^{+0.3}_{-0.4}$	$0^{+0.4}_{-0.5}$
$E_{\rm cut}$	15.2 ± 0.03	$12.2^{+0.8}_{-0.9}$	17.3 ± 1.1	13.4 ± 0.6	16.1 ± 0.7	$14.6^{+1.2}_{-1.5}$	$16.3^{+0.8}_{-1.3}$	16.0 ± 0.7	15.7 ± 0.8	$15.5^{+1.4}_{-1.2}$	$15.2^{+4.1}_{-3.9}$	$16.8^{+5.9}_{-3.5}$	$14.3^{+1.5}_{-1.3}$
$E_{\rm fold}$	6.8 ± 0.03	$4.6^{+1.0}_{-0.8}$	7.2 ± 1.3	$3.9^{+0.7}_{-0.5}$	4.7 ± 0.6	$6.2^{+1.6}_{-0.8}$	$5.8^{+0.9}_{-0.7}$	6.9 ± 0.8	7.0 ± 0.8	$6.3^{+2.0}_{-1.4}$	8.5 ± 4.6	$6.0^{+6.2}_{-6.0}$	$7.1^{+2.5}_{-1.6}$
$F_{0.5-10\ \rm keV}$	1.61E-11	1.8E-12	6.3E-11	5.0E-11	2.2E-10	7.9E-10	2.3E-9	1.6E-9	7.6E-10	5.6E-10	3.8E-10	3.1E-11	1.7E-11
$F_{10-30\ \rm keV}$	1.98E-11	2E-12	1.3E-10	1.3E-10	4.6E-10	1.3E-9	3.7E-9	2.5E-9	1.3E-9	9.9E-10	6.4E-10	8.3E-11	3.1E-11
$\chi^2_{\rm red}$/d.o.f.	1.11/986	1.09/479	1.27/414	1.07/331	0.94/338	1.04/248	0.91/368	1.04/607	0.91/536	1.04/208	0.90/185	0.86/210	1.06/258
$C_{\rm pn}$	—	1.0	1.00 ± 0.05	1.03 ± 0.06	0.97 ± 0.05	0.95 ± 0.07	0.98 ± 0.06	0.97 ± 0.04	1.03 ± 0.04	1.02 ± 0.08	0.98 ± 0.07	0.94 ± 0.05	1.00 ± 0.05
$C_{\rm MOS1}$	—	1.12 ± 0.03	0.96 ± 0.07	1.01 ± 0.08	1.03 ± 0.10	0.85 ± 0.17	—	—	—	—	—	0.90 ± 0.09	1.0[c]
$C_{\rm MOS2}$	1.0	1.34 ± 0.03	1.0	1.0	1.0	1.0	1.0	1.0	1.0	1.0	1.0	1.0	1.0
$C_{\rm RGS1}$	1.21 ± 0.07	—	—	—	—	—	—	—	—	—	—	—	—
$C_{\rm RGS2}$	1.10 ± 0.10	—	—	—	—	—	—	—	—	—	—	—	—
$C_{\rm FPMA}$	0.75 ± 0.01	0.93 ± 0.04	0.99 ± 0.07	1.06 ± 0.09	1.08 ± 0.07	1.01 ± 0.07	1.08 ± 0.06	1.11 ± 0.04	1.08 ± 0.05	1.14 ± 0.10	0.95 ± 0.08	1.6 ± 0.2	1.00 ± 0.09
$C_{\rm FPMB}$	0.79 ± 0.02	1.11 ± 0.09	1.05 ± 0.07	1.03 ± 0.06	1.14 ± 0.07	1.00 ± 0.07	1.13 ± 0.06	1.11 ± 0.04	1.11 ± 0.5	1.14 ± 0.09	1.00 ± 0.09	1.8 ± 0.2	1.01 ± 0.10

Notes. In each case, the normalization constant with no indicated uncertainties is the one of the instrument used as a reference in the fit. [(a)] For these spectra a thin iron line was also included in the fit. The centroid energy of the line is 6.39 ± 0.03 keV and the corresponding equivalent width is 0.073 ± 0.016 keV. [(b)] For these spectra we also included in the fit an absorption line at 7.21 ± 0.14 keV with an equivalent width of $0.23^{+0.11}_{-0.06}$ keV and a width of 0.2 ± 0.1 keV. [(c)] This value was fixed in the fit as the fit was insensitive to any variation of this parameter within reasonable boundaries.

blackbody processes taking place within an accreting plasma, characterized by a constant magnetic field and electron density. In this situation, the distributions in energy of the cyclotron and bremsstrahlung photons are generally different. However, in those cases where the cyclotron energy is comparable to the temperature of the plasma, the cyclotron emission becomes the preferred cooling channel. The blackbody emission is assumed to be concentrated toward the bottom of the accretion column. We refer the reader to Ferrigno et al. (2009) and Becker & Wolff (2007) for further details.

The BW model has six free parameters[3]: the mass accretion rate $\dot{M}$, the radius of the accretion column r_0, the temperature of the electrons $T_{\rm e}$, the magnetic field strength B, the

[3] In all cases, we fixed the NS mass and radius to the canonical values, $M_{\rm NS}$ = 1.4 $M_\odot$ and $R_{\rm NS}$ = 10^6 cm. These parameters could not be constrained in any of the fits.

Table 4. Results of the fits to the combined *XMM-Newton* and *NuSTAR* spectra with the physical model introduced in Sect. 4.

Parameter	3	4	5	6	7	8	9
$N_{\rm H}$ (1E22 cm^{-2})	$1.9^{+0.3}_{-0.2}$	$1.3^{+0.3}_{-0.2}$	$1.2^{+0.2}_{-0.3}$	$1.2^{+0.2}_{-0.3}$	1.1 ± 0.1	1.0 ± 0.4	1.0 ± 0.3
$kT_{\rm BB}$ (keV)	1.5 ± 0.1	1.7 ± 0.2	1.6 ± 0.3	1.5 ± 0.2	1.4 ± 0.1	$1.4^{+0.4}_{-0.2}$	1.2 ± 0.2
$N_{\rm BB}$	$3.9^{+0.7}_{-0.5}$	$8.3^{+3.1}_{-2.1}$	25^{+18}_{-10}	$19.3^{+9.2}_{-6.3}$	$13.6^{+6.0}_{-3.2}$	$8.9^{+8.3}_{-5.3}$	$11.4^{+6.1}_{-3.6}$
ξ	$5.0^{+8.0}_{-0.7}$	<15	$4.5^{+4.2}_{-3.0}$	$5.4^{+3.6}_{-2.5}$	$5.7^{+6.8}_{-5.0}$	$5.7^{+6.6}_{-3.6}$	<5.2
δ	$0.8^{+0.2}_{-0.4}$	$0.4^{+0.5}_{-0.2}$	$0.7^{+0.9}_{-0.3}$	$0.6^{+0.5}_{-0.3}$	$0.3^{+0.4}_{-0.1}$	$0.7^{+0.8}_{-0.5}$	<1.0
$\dot{M}^{a}_{1E17{\rm g/s}}$	0.05	0.17	0.48	0.32	0.16	0.12	0.08
$T_{\rm e}$ (keV)	$3.2^{+0.3}_{-0.2}$	3.4 ± 0.3	$2.9^{+0.3}_{-0.4}$	3.0 ± 0.3	3.4 ± 0.3	$2.8^{+0.6}_{-0.4}$	$3.7^{+0.9}_{-0.7}$
r_0 (m)	<20	47^{+14}_{-25}	65 ± 33	53^{+21}_{-18}	35^{+18}_{-23}	18^{+22}_{-18}	19^{+28}_{-19}
$F^{b}_{0.-10\ {\rm keV}}$	2.2E-10	7.8E-10	2.4E-9	1.6E-9	7.6E-10	5.6E-10	3.8E-10
$F^{b}_{10-30\ {\rm keV}}$	4.6E-10	1.3E-9	3.6E-9	2.5E-9	1.3E-9	9.7E-10	6.6E-10
$\chi^2_{\rm red}$/d.o.f.	0.94/338	1.03/248	0.92/375	1.08/605	0.93/534	1.05/207	0.90/185
$C_{\rm pn}$	0.96 ± 0.05	0.96 ± 0.07	0.95 ± 0.05	0.97 ± 0.04	1.04 ± 0.04	1.02 ± 0.07	0.98 ± 0.07
$C_{\rm MOS1}$	1.0 ± 0.1	1.0 ± 0.1	–	–	–	–	–
$C^{c}_{\rm MOS2}$	1.0	1.0	1.0	1.0	1.0	1.0	1.0
$C_{\rm FPMA}$	1.08 ± 0.08	1.02 ± 0.07	1.06 ± 0.06	1.11 ± 0.04	1.07 ± 0.04	1.14 ± 0.09	0.95 ± 0.09
$C_{\rm FPMB}$	1.13 ± 0.07	1.02 ± 0.07	1.11 ± 0.06	1.11 ± 0.04	1.11 ± 0.05	1.13 ± 0.09	1.00 ± 0.08

Notes. [(a)] The mass accretion rate is derived from the 0.5–30 keV X-ray flux using standard equations for the NS accretion, that is, $L_{\rm X} = GM_{\rm NS}\dot{M}/R_{\rm NS}$ and $L_{\rm X} = 4\pi F_{0.5-30\ {\rm keV}} d^2$ (here $M_{\rm NS}$ and $R_{\rm NS}$ are the mass and radius of the NS, whilst d is the source distance). [(b)] The flux is given in erg cm^{-2} s^{-1}. [(c)] The MOS2 was used in all case as the reference instrument, therefore the corresponding normalization constant has been fixed to unity.

photon diffusion parameter ξ, and the Comptonization parameter δ. The last two parameters are defined as:

$$\xi = \frac{\pi r_0 m_{\rm p} c}{\dot{M}(\sigma_{\parallel}\sigma_{\perp})^{1/2}}, \quad (1)$$

$$\delta = 4\frac{y_{\rm bulk}}{y_{\rm thermal}}, \quad (2)$$

where $m_{\rm p}$ is the proton mass, c is the speed of light, $\sigma_{\parallel}$, ($\sigma_{\perp}$) is the electron scattering cross section for photons propagating parallel (perpendicular) to the magnetic field direction, and $y_{\rm bulk}$ ($y_{\rm thermal}$) describes the average fractional energy change experienced by a photon before it escapes through the walls of the accretion column due to the bulk (thermal) Comptonization. As in this model the normalization is regulated by both $\dot{M}$ and r_0 and in all fits we fixed the value of the mass accretion rate to the one estimated from the source broad-band X-ray luminosity (0.5–30 keV) with the usual formula $L_{\rm X} = GM_{\rm NS}\dot{M}/R_{\rm NS}$ and left r_0 free to vary.

Due to all physical assumptions in the treatment presented by Becker & Wolff (2007), the BW model is only suited to describe the X-ray energy distribution of X-ray pulsars with a luminosity larger than a certain critical value. The latter corresponds to the luminosity at which the radiation emerging from the NS surface is able to stop the accreting matter infalling through the accretion column via a radiation-dominated shock. The precise value of this critical luminosity is highly debated, but the most recent calculations presented by Mushtukov et al. (2015) show that it should not be lower than $\sim 2 \times 10^{36}$ erg s^{-1} for a NS endowed with a magnetic field similar to that suspected for IGR J17544-2619 (i.e. $\sim 1.5 \times 10^{12}$ G, see Sect. 1). At the distance of IGR J17544-2619, the above luminosity corresponds to an X-ray flux of $\sim 10^{-9}$ erg cm^{-2} s^{-1}. Based on the results obtained in Sect. 3 and on the considerations above, we thus performed fits to spectra 3–9 in Table 3 with the BW model only. A blackbody was included in all fits to take into account the presence of the thermal component emitted from the BW model. The results of these fits are summarized in Table 4. We note that the measured parameters of the BW model are comparable to the values expected for a highly magnetized NS ($\sim 10^{12}$ G). The estimated radius of the accretion column is substantially lower than that measured in the case of the brightest X-ray pulsars (up to several hundreds of meters; see, e.g., Walter et al. 2015, and references therein), but in line with the prediction for dimmer systems, such as Her X-1 (Becker & Wolff 2007).

On the right side of Fig. 7 we show a comparison between the fits with the physical and phenomenological models to the spectra 6 and 9, as these were previously considered as two representative cases for the spectral changes occurring in the source X-ray emission during the decay from the second flare (when the most prominent spectral variability was recorded).

5. Optical and infrared observations

We also obtained optical and infrared data during the long observations performed with *XMM-Newton* and *NuSTAR*. Data were collected with:

- the Berlin Exoplanet Search Telescope (BEST II), which is a 25 cm aperture Baker-Ritchey-Chrétien system, using a KAF 16801 4096 × 4096 pixel CCD with a pixel size of 9 μm and a field of view of 1.7° × 1.7° (see, Kabath et al. 2009, for all relevant information);
- the Bochum Monitoring Telescope[4] (BMT), which is a 40 cm Coudé telescope, featuring a SBIG STL-6303 CCD with 3072 × 2048 pixel (each sized 9 μm) with a field of view of 41.2′ × 27.5′ (Ramolla et al. 2013);

[4] http://www.astro.rub.de/Astrophysik/BMT_en.html

Table 5. Log of optical and NIR observations of IGR J17544-2619.

Filter	Telescope	Start time (UT)	End time (UT)	Exp time (s)
$B-V$	BMT	8:25:58	08:57:16	1900
$R-I$	BEST	08:35:51	09:18:12	2600
$Ks-Jn$	IRIS	09:06:58	10:06:52	3600

Table 6. Results obtained from the optical and NIR photometry of IGR J17544-2619.

Filter	N frames	Exp. time (s)	Magnitude	
			(This work)	(Literature)
B	11	60	14.62 ± 0.05	14.44 ± 0.05^a
V	7	60	12.89 ± 0.05	12.65 ± 0.05^a
R	9	60	11.76 ± 0.05	$<11.9^a$
I	9	60	10.39 ± 0.05	
Jn	20	10	8.77 ± 0.05	8.71 ± 0.02^a; 8.791 ± 0.021^b
Ks	20	10	8.21 ± 0.05	7.99 ± 0.02^a; 8.018 ± 0.026^b

Notes. [(a)] Data from Pellizza et al. (2006). [(b)] Data from the 2MASS catalogue (Skrutskie et al. 2006).

– the Infrared Imaging System (IRIS) telescope, which is a 80 cm Nasmyth telescope equipped with a HAWAII-1 detector. The telescope field of view is $12.5' \times 12.5'$ (with a pixel size of $0''.74 \times 0''.74$), and a filter wheel equipped with standard 2MASS J, H, K and narrow band filters (Hodapp et al. 2010).

IGR J17544-2619 was observed with all mentioned instruments on 2015 March 21 in Johnson BVRI filters and 2MASS Jn and Ks filters. The coverage in the different filters is specified in Table 5. All photometric data were reduced using standard Image Reduction and Analysis Facility (IRAF) bias, dark, and flat field correction routines. Astrometry was provided by SCAMP (Bertin 2006) and before combining a set of multiple exposures into a final frame, the data were re-sampled onto a common WCS frame using SWARP (Bertin et al. 2002). The photometry was performed on combined frames using a $7''.5$ aperture. To obtain absolute calibration in the optical bands, the Landolt star fields SA 104 and SA 107 (Landolt 2009) were observed. The field star fluxes were cross-calibrated with the Landolt photometry, taking into account the airmass dependent extinction based on the atmospheric profile of the Cerro Paranal site obtained by Patat et al. (2011). In the infrared, available 2MASS AAA photometry of field stars in our frames was used to directly cross calibrate the photometry.

We report all photometric results of the averaged frames with min/max rejection in Table 6. The magnitude of the source in the observations with different filters was estimated using isolated field stars and the UCAC-4 photometry. In the Table we indicate the exposure time of single frame observations for each filter and the number of frames combined in each case to obtain the final results. For comparison we also report the results on all filters that we could find in the literature for IGR J17544-2619.

As all the optical and IR observations of IGR J17544-2619 were obtained several hours before the bright outburst from the source detected by *XMM-Newton* and *NuSTAR*, the results reported in Table 6 describe the properties of the supergiant companion when the system was in a quiescent state. Comparison with previous results in the literature reveals that the supergiant was globally fainter during our observations. However, the differences with the previously reported magnitudes are very limited and likely consistent with the micro-variability observed in other supergiant systems (see, e.g, the case of IGR J16465-4507; Chaty et al. 2016).

6. Discussion

In this paper we report on a long multi-wavelength campaign observation of the SFXT prototype IGR J17544-2619. This source is known to display one of the most extreme levels of X-ray variability among other objects in the same class. A remarkable dynamic range in the X-ray luminosity was also observed.

IGR J17544-2619 was initially caught by both *XMM-Newton* and *NuSTAR* during an extended quiescent period, which covered the first ~120 ks of the observations and was characterized by a luminosity of $\sim 6 \times 10^{33}$ erg s^{-1}. During this period the statistics of the data were too low to carry out a time-resolved spectral analysis, and thus a single spectrum was extracted for all *XMM-Newton* instruments and for the two FMs of *NuSTAR*. The source spectral energy distribution in the X-ray domain could be well-described by using a combination of a thermal component, most likely associated with the emission from the neutron star surface, and a non-thermal component extending up to ~40 keV. The latter is usually ascribed in similar systems to Comptonization processes occurring within the accretion column of the neutron star. The peculiarly high emission around 10–20 keV made it very difficult to fit the non-thermal component with any other phenomenological model other than the HIGHECUT*POW in XSPEC. This model provided reasonably good fit to all spectra extracted from both the *XMM-Newton* and *NuSTAR* data.

A bright outburst abruptly interrupted the source quiescent state towards the end of the X-ray observations and lasted for approximately 7 ks. The event comprised three distinct fast flares, among which the first was the faintest and the other two achieved a luminosity $\gtrsim$1600 times brighter than quiescence. Significant spectral variability was observed, especially during the second flare. In particular, the broad-band fits realized by combining the time-resolved *XMM-Newton* and *NuSTAR* data showed that there was a modest (but significant) increase of the absorption column density during the rise to the peak of the flare (a factor of ~1.5), followed by a drop of the column density immediately after the source reached the peak X-ray flux. This is reminiscent of what was observed during the bright flare from the SFXT IGR J18410-0535 (Bozzo et al. 2011). On that occasion the increase in the absorption column density during the onset of the flare was much larger (by a factor of ~50) however it was also observed to drop significantly at the peak of the event. The interpretation in this case was that a large clump in the wind of the supergiant companion encountered the neutron star and partially obscured the X-ray source before being accreted onto the compact object. The increase in the absorption column density and the total X-ray luminosity released during the flare were used to estimate the physical projected size of the clump and its mass. The drop in the absorption column density around the peak of the flare could be explained by assuming that the clump material became significantly ionized when the incident X-ray radiation exceeded a certain threshold.

The above interpretation could also be applied to explain the event observed from IGR J17544-2619. However, why a much lower increase in the column density was measured in the present case compared to the flare displayed by IGR J18410-0535 remains puzzling, although the peak flux in the latter event was

approximately a factor of ten lower than that recorded during the outburst of IGR J17544-2619. A viable solution could be to assume that the flare from IGR J17544-2619 was observed from an unfavorable geometry in which the clump approaching the neutron star was not located along the line of sight to the observer and thus gave rise to a limited increase in the measured absorption column density. The presence of different flares within the same outburst could be ascribed to the presence of structured clumps or to the accretion of multiple smaller clumps impacting one after the other onto the compact object (Walter & Zurita Heras 2007).

This scenario would be in line with our current understanding of the SFXT phenomenology (see Sect. 1), however the current consensus is that clumps alone cannot be the sole explanation for all the peculiar properties of the X-ray behavior of these sources (see, e.g., Bozzo et al. 2015). It remains particularly difficult to explain why IGR J17544-2619, as well as other SFXTs, displays on average a much lower luminosity compared to the value that would be expected if they were classical SgXBs. The monitoring we performed with XRT during the entire orbital revolution of IGR J17544-2619, during which also the *XMM-Newton* and *NuSTAR* observations were carried out, showed that the source remained in a relatively faint X-ray state for most of the time. The average flux of 2.7×10^{-12} erg cm^{-2} s^{-1} recorded by XRT corresponds to an X-ray luminosity of 4×10^{33} erg s^{-1} at the distance of IGR J17544-2619. As pointed out by Romano et al. (2014a) and Bozzo et al. (2015), this is orders of magnitudes lower than the luminosity expected from a classical wind-fed SgXBs having similar orbital parameters to those of IGR J17544-2619 (see also Lutovinov et al. 2013). It should thus be argued that some mechanism is at work in the SFXTs inhibiting accretion for most of the time. Among the different possibilities proposed so far and summarized in Sect. 1, none seem able to satisfactorily explain all observational properties shown by all SFXTs so far. As discussed in Walter et al. (2015), it is unlikely that the settling accretion regime alone could produce a dynamic X-ray range as high as the one displayed by IGR J17544-2619, as it would require a large systematic difference in the stellar winds of the SFXT supergiant companions with respect to those in classical systems which seem not to be supported by the available observations. The gating models typically require a large neutron star magnetic field to be able to reproduce an SFXT-like behavior. As it was recently shown by Bozzo et al. (2016), it is particularly challenging to explain within the assumptions of this model the onset of very sporadic bright outbursts if the neutron star magnetic field is not $\gtrsim 10^{13}$–10^{14} G. Although in the present paper we could not confirm the presence of a cyclotron line in the X-ray spectrum of IGR J17544-2619 as found previously by Bhalerao et al. (2015), the detection of this feature is not affected by the specific model adopted to fit the source broad-band spectrum, and thus the estimate of the source's relatively low magnetic field ($B \simeq 1.5 \times 10^{12}$ G) seems robust. At present, we thus conclude that the X-ray behavior displayed by IGR J17544-2619 (as well as by the other extreme SFXTs) is challenging all presently proposed theoretical models[5] and a satisfactorily explanation for the exceptional X-ray variability of this object requires additional progress in the development of current models.

Assuming that the neutron star hosted in IGR J17544-2619 is similar to the X-ray pulsars identified in many other SgXBs and high mass X-ray binaries (HMXBs) in general, we also attempted to model its high energy emission in Sect. 4 with the physical model proposed by Becker & Wolff (2007) plus the contribution of the thermal emission coming from the neutron star surface. In the BW model the higher energy photons are produced by the free-free interactions in the magnetic field of the pulsar and then up-scattered within the accretion column. With a neutron star magnetic field of $\sim 10^{12}$ G, electrons in the accretion stream populate the first Landau level by collisional excitation, largely affecting the X-ray spectrum emerging from the column. Calculations by Riffert & Meszaros (1988) showed that in the optically thin regime an enhanced emission is produced at energies close to the local cyclotron energy, while the thermal breemstrahlung dominates the emission at much lower energies. In the simplified approach of Becker & Wolff (2007), the breemstrahlung and the cyclotron emission are considered as separate contributions in order to linearize an otherwise very complicated process. For the input spectrum these authors assume a thermal breemstrahlung as well as a delta-shaped emission for the cyclotron component. The Comptonization of both components within the accretion column is then realized through a Green's function that takes into account the thermal and bulk Comptonization. The implementation of the BW model[6] within XSPEC was discussed by Ferrigno et al. (2009) and first tested on the HMXB 4U 0115+63. The pronounced emission detected from IGR J17544-2619 around 10–20 keV, which was highlighted in Sect. 3 as a peculiar feature of the source spectral energy distribution, is elegantly reproduced in the BW model by the broadened cyclotron emission. This corresponds to the large peak visible in the right-hand plots of Fig. 7 that covers approximately the energy range 10–20 keV. Note that, as should be expected in this model, the broadened cyclotron emission is centered around the centroid energy of the cyclotron feature previously detected in the X-ray spectrum of IGR J17544-2619 (Bhalerao et al. 2015).

It should be remarked that the Comptonization of the black body seed photons coming from the base of the accretion column and self-consistently accounted for in the BW model yields a negligible contribution to the computed X-ray emission. As discussed in Ferrigno et al. (2009), the presence of an evident, additional soft thermal component in the spectrum of the source can be interpreted assuming the presence of an extended halo on the NS surface. This could be produced by either material arriving on regions of the neutron star surface external to the column during the accretion process or photons in the accretion stream that heat a sufficiently large fraction of the neutron star surface. From the results of the time resolved spectral analysis carried out with the BW model (see Table 4), we can conclude that the relative intensity of the black-body and cyclotron emission components varies with the source luminosity, with the black-body being more prominent when the source is dimmer. This is compatible with the behavior of thermal and non-thermal components observed in other X-ray pulsars (see Ferrigno et al. 2009, and references therein) and with our interpretation that the black-body emission is due to the continuous heating of the neutron star surface. We mentioned in Sect. 4 that the spectral parameters measured from the fits of the physical model to the combined *XMM-Newton* and *NuSTAR* data lie

[5] We note that the suggestion by Giménez-García et al. (2016) according to which IGR J17544-2619 could spend most of its time in the so-called supersonic propeller regime critically depends on the value of the source spin period, a parameter that is not known yet (two values were suggested so far and never confirmed, see Sect. 1).

[6] http://www.isdc.unige.ch/~ferrigno/images/Documents/BW_distribution/BW_cookbook.html.

between the usual boundaries determined for a number of other highly magnetized X-ray pulsars (see, e.g., Walter et al. 2015, and references therein) and therefore cannot easily help in understanding why SFXTs behave in such an atypical way compared to other wind-fed HMXBs. As discussed and analyzed by Shakura et al. (2013), the pulse profile of these sources, together with their energy and time dependence, are probes of the different accretion mechanisms and geometries. This could help to discriminate among the different theoretical models proposed to interpret the SFXT behavior, however these investigations are at present hampered by the lack of spin period measurements for most of the SFXTs (see Sect. 1). Longer and deeper X-ray observations are thus needed in order to eventually confirm the tentative spin period detections reported for IGR J17544-2619 and to sensitively search for pulsations in all other SFXTs. Note that the presence of a hot, relatively confined black-body component on the surface of the NS hosted in IGR J17544-2619, as well as in a number of other SFXTs, would suggest that pulsations can be expected from these sources and might have gone undetected so far mostly due to the very long spin period (see, e.g., Bozzo et al. 2008, 2010; Sidoli et al. 2009, and references therein). A similar conclusion was reached by Walter & Ferrigno (2016), who proposed that the spacing among the different flares usually detected within the SFXT structured outbursts (generally a few ks) could be an indication of the NS spin period. If the magnetic and rotation axes of the NS are closely aligned and the radiation is beamed in unfavourable directions, then we might only be able to see pulsations during the brightest outbursts, while for most of the time the source remains barely detectable.

Interestingly, if we use the most recent ephemeris available for IGR J17544-2619 (orbital period 4.92693 ± 0.00036 d and periastron passage at $53\,732.65 \pm 0.23$ MJD; Smith 2014), it turns out that the bright outburst observed by *XMM-Newton* and *NuSTAR* falls at the expected phase of the pariastron passage. This confirms previous findings that most of the outbursts displayed by IGR J17544-2619 occur when the neutron star is closer to the supergiant companion and that the orbit of this system could be characterized by a non-negligible eccentricity (see, e.g., Drave et al. 2014; Romano 2015, and references therein). Although this eccentricity could help in enhancing the X-ray dynamic range achievable by IGR J17544-2619, it cannot be the only explanation for the extreme behavior displayed by this source, as the system orbital period is relatively short and only a limited eccentricity of $\lesssim 0.2-0.3$ can be expected (Walter et al. 2015; Giménez-García et al. 2016).

In SFXTs with orbital periods of only a few days and characterized by a non-negligible eccentricity, as for example IGR J17544-2619 and IGR J16479-4514, it was suggested that the neutron star could get close enough to the supergiant to largely slow down its wind through X-ray photoionization and lead to the formation of temporary accretion disks (see Ducci et al. 2010, and references therein). In the case of IGR J17544-2619, the presence of such structures was first suggested by Romano et al. (2015) based on the peak luminosity achieved during an outburst on 2014 October 10 that was too high to be produced within a wind-fed system. No direct evidence of disks in SFXTs has been reported so far. In the *XMM-Newton* observations of IGR J17544-2619 during the time interval 10 (see Fig. 2) we found an intriguing feature at 7.2 keV. This is reminiscent of the iron absorption lines usually observed in high inclination low mass X-ray binaries when material is pulled out from the disk and the X-ray radiation passes through it, ionizing this absorber before arriving at the observer (see, e.g., Díaz Trigo & Boirin 2013, and references therein). On one hand, the presence of this feature could indicate the presence of at least a temporary disk-like structure[7] around the neutron star in IGR J17544-2619, opening up the possibility that a different accretion mechanism, poorly explored so far, could play a role in regulating the SFXT X-ray variability. On the other hand, it is quite unlikely that IGR J17544-2619 is observed at high inclination angles, as the system is characterized by a relatively small orbital separation but no eclipses are detected in its long term lightcurve (Romano et al. 2014b). An alternative possibility is that the material filtering the X-ray radiation could be associated with the clump being accreted and ionized during the first two flares of the source X-ray outburst. While this interpretation is much more in line with the scenario depicted above to interpret the overall behavior displayed by IGR J17544-2619, we remark that (to the best of our knowledge) no similar features have so far been observed in other wind-fed HMXBs. The limited statistics of the *XMM-Newton* data during the relatively short and faint time interval 10, combined with the lack of complete coverage of this interval by *NuSTAR*, have prevented us from performing a more refined study of this feature.

Finally, we also reported on the results of optical and IR observations carried out during the same orbital revolution of IGR J17544-2619 observed in X-rays with *Swift*/XRT, *XMM-Newton*, and *NuSTAR*. These additional observations captured the system during the quiescent period and did not reveal any peculiar changes in the properties of the supergiant companion that could provide help in investigating the mechanism triggering the bright outburst observed in X-rays. The measured limited changes in the optical and IR magnitudes of the source are compatible with the expected micro-variability of supergiant stars. A similar consideration applies to the UVOT data in the UV energy range, which provided measurements of the magnitudes in different filters compatible with previous results reported in the literature. We note that the results of more extended UVOT photometric monitoring campaigns of the SFXTs were reported previously by Romano et al. (2011) and Romano (2015), for example. These authors found similar results, with no significant evidence of changes in the magnitudes of the supergiant stars in the SFXTs even close to the epoch of the different outbursts caught by *Swift*. Strictly simultaneous and fast (few seconds) optical, IR, and UV measurements during the X-ray outburst carried out with large telescopes could help investigate the presence of particularly massive clumps impacting against the neutron star. However, scheduling these observations is very challenging as the precise occurrence of SFXT outbursts cannot be predicted a priori and many periastron passages of IGR J17544-2619 are observed where no X-ray outburst is taking place (see the discussion in, e.g., Drave et al. 2014). The investigation of the spectral properties, rather than of only the photometric variations, of the SFXT supergiant companions in the optical, infrared, and ultraviolet domain has been shown to be able to provide some useful information on the characteristics of their stellar winds compared to those in classical systems (Giménez-García et al. 2016). However, precise measurements of the wind properties are still scarce due to the large distances of the SFXTs that make observations challenging, especially in

[7] In principle, the iron emission line detected when the *XMM-Newton* and *NuSTAR* data are averaged over the entire observational period could also be formed in an accretion disk. However, the fact that the line is thin and compatible with what is usually observed from other SFXTs and wind-fed HMXBs suggests that it is more likely produced due to fluorescence in the supergiant wind material surrounding the compact object and illuminated by its X-ray emission (see, e.g., Walter et al. 2015).

the ultraviolet domain. Furthermore, through the performed observational campaigns so far, it was not possible to identify a net difference in the stellar wind properties of SFXTs and classical SgXBs, and thus the tentative discrimination between the proposed theoretical scenarios in the two classes of sources still relies upon the largely unknown values of the neutron star pulsation periods and magnetic field strength (see discussions in Bozzo et al. 2016; Giménez-García et al. 2016).

Acknowledgements. We warmly thank the *XMM-Newton* and *NuSTAR* teams for their efforts in scheduling the simultaneous observations of IGR J17544-2619. This work was supported under NASA Contract No. NNG08FD60C, and made use of data from the *NuSTAR* mission, a project led by the California Institute of Technology, managed by the Jet Propulsion Laboratory, and funded by the National Aeronautics and Space Administration. This research has made use of the *NuSTAR* Data Analysis Software (NuSTARDAS) jointly developed by the ASI Science Data Center (ASDC, Italy) and the California Institute of Technology (USA). We also made use of observations obtained with *XMM-Newton*, an ESA science mission with instruments and contributions directly funded by ESA Member States and NASA. This publication was motivated by a team meeting sponsored by the International Space Science Institute in Bern, Switzerland. E.B., L.O., and A.M. thank ISSI for their financial support during their stay in Bern. V.B. and J.A.T. thank Brian Grefenstette and Kristin Madsen for help with planning the NuSTAR observations and Lorenzo Natalucci and David Smith for useful discussions. P.R. acknowledges contract ASI-INAF I/004/11/0 and financial contribution from the agreement ASI-INAF I/037/12/0. A.M. acknowledges support from the Polish NCN grant 2013/08/A/ST9/00795. S.C. is grateful to the Centre National d'Études Spatiales (CNES) for the funding of MINE (Multi-wavelength INTEGRAL Network). We thank the anonymous referee for detailed and useful referee report that helped improve the paper.

References

Bachetti, M., Harrison, F. A., Cook, R., et al. 2015, ApJ, 800, 109
Becker, P. A., & Wolff, M. T. 2007, ApJ, 654, 435
Bertin, E. 2006, in Astronomical Data Analysis Software and Systems XV, eds. C. Gabriel, C. Arviset, D. Ponz, & S. Enrique, ASP Conf. Ser., 351, 112
Bertin, E., Mellier, Y., Radovich, M., et al. 2002, in Astronomical Data Analysis Software and Systems XI, eds. D. A. Bohlender, D. Durand, & T. H. Handley, ASP Conf. Ser., 281, 228
Bhalerao, V., Romano, P., Tomsick, J., et al. 2015, MNRAS, 447, 2274
Bozzo, E., Falanga, M., & Stella, L. 2008, ApJ, 683, 1031
Bozzo, E., Stella, L., Ferrigno, C., et al. 2010, A&A, 519, A6
Bozzo, E., Giunta, A., Cusumano, G., et al. 2011, A&A, 531, A130
Bozzo, E., Romano, P., Ferrigno, C., et al. 2013, A&A, 556, A30
Bozzo, E., Romano, P., Ducci, L., Bernardini, F., & Falanga, M. 2015, Adv. Space Res., 55, 1255
Bozzo, E., Oskinova, L., Feldmeier, A., & Falanga, M. 2016, A&A, 589, A102
Breeveld, A. A., Landsman, W., Holland, S. T., et al. 2011, in AIP Conf. Ser., 1358, eds. J. E. McEnery, J. L. Racusin, & N. Gehrels, 373
Chaty, S., LeReun, A., Negueruela, I., et al. 2016, A&A, 591, A87
Clark, D. J., Hill, A. B., Bird, A. J., et al. 2009, MNRAS, 399, L113
Coburn, W., Heindl, W. A., Gruber, D. E., et al. 2001, ApJ, 552, 738
Davies, R. E., & Pringle, J. E. 1981, MNRAS, 196, 209
Díaz Trigo, M., & Boirin, L. 2013, Acta Polytechnica, 53, 659
Drave, S. P., Bird, A. J., Townsend, L. J., et al. 2012, A&A, 539, A21
Drave, S. P., Bird, A. J., Sidoli, L., et al. 2014, MNRAS, 439, 2175
Ducci, L., Sidoli, L., & Paizis, A. 2010, MNRAS, 408, 1540
Ferrigno, C., Becker, P. A., Segreto, A., Mineo, T., & Santangelo, A. 2009, A&A, 498, 825
Giménez-García, A., Torrejón, J. M., Eikmann, W., et al. 2015, A&A, 576, A108
Giménez-García, A., Shenar, T., Torrejón, J. M., et al. 2016, A&A, 591, A26
Grebenev, S. A., & Sunyaev, R. A. 2007, Astron. Lett., 33, 149
Hodapp, K. W., Chini, R., Reipurth, B., et al. 2010, in Ground-based and Airborne Instrumentation for Astronomy III, Proc. SPIE, 7735, 77351A
in't Zand, J. J. M. 2005, A&A, 441, L1
Kabath, P., Erikson, A., Rauer, H., et al. 2009, A&A, 506, 569
Kraft, R. P., Burrows, D. N., & Nousek, J. A. 1991, ApJ, 374, 344
Landolt, A. U. 2009, AJ, 137, 4186
Lutovinov, A. A., Revnivtsev, M. G., Tsygankov, S. S., & Krivonos, R. A. 2013, MNRAS, 431, 327
Manousakis, A., & Walter, R. 2011, A&A, 526, A62
Mushtukov, A. A., Suleimanov, V. F., Tsygankov, S. S., & Poutanen, J. 2015, MNRAS, 447, 1847
Negueruela, I., Smith, D. M., Harrison, T. E., & Torrejón, J. M. 2006, ApJ, 638, 982
Oskinova, L. M., Feldmeier, A., & Kretschmar, P. 2012, MNRAS, 421, 2820
Patat, F., Taubenberger, S., Benetti, S., Pastorello, A., & Harutyunyan, A. 2011, A&A, 527, L6
Pellizza, L. J., Chaty, S., & Negueruela, I. 2006, A&A, 455, 653
Rahoui, F., Chaty, S., Lagage, P., & Pantin, E. 2008, A&A, 484, 801
Ramolla, M., Drass, H., Lemke, R., et al. 2013, Astron. Nachr., 334, 1115
Rampy, R. A., Smith, D. M., & Negueruela, I. 2009, ApJ, 707, 243
Riffert, H., & Meszaros, P. 1988, ApJ, 325, 207
Romano, P. 2015, J. High Energy Astrophysics, 7, 126
Romano, P., La Parola, V., Vercellone, S., et al. 2011, MNRAS, 410, 1825
Romano, P., Ducci, L., Mangano, V., et al. 2014a, A&A, 568, A55
Romano, P., Krimm, H. A., Palmer, D. M., et al. 2014b, A&A, 562, A2
Romano, P., Bozzo, E., Mangano, V., et al. 2015, A&A, 576, L4
Roming, P. W. A., Kennedy, T. E., Mason, K. O., et al. 2005, Space Sci. Rev., 120, 95
Sguera, V., Bazzano, A., Bird, A. J., et al. 2006, ApJ, 646, 452
Shakura, N., Postnov, K., Kochetkova, A., & Hjalmarsdotter, L. 2012, MNRAS, 420, 216
Shakura, N., Postnov, K., & Hjalmarsdotter, L. 2013, MNRAS, 428, 670
Sidoli, L., Romano, P., Ducci, L., et al. 2009, MNRAS, 397, 1528
Skrutskie, M. F., Cutri, R. M., Stiening, R., et al. 2006, AJ, 131, 1163
Smith, D. M. 2014, ATel, 6227
Sunyaev, R. A., Grebenev, S. A., Lutovinov, A. A., et al. 2003, ATel, 190, 1
Torrejón, J. M., Schulz, N. S., Nowak, M. A., & Kallman, T. R. 2010, ApJ, 715, 947
Tueller, J., Barthelmy, S., Burrows, D., et al. 2005, ATel, 669, 1
Walter, R., & Ferrigno, C. 2016, ArXiv e-prints [arXiv:1608.06530]
Walter, R., & Zurita Heras, J. 2007, A&A, 476, 335
Walter, R., Lutovinov, A. A., Bozzo, E., & Tsygankov, S. S. 2015, A&ARv, 23, 2
White, N., Nagase, F., & Parmar, A. 1995, in X-ray Binaries, eds. W. H. G. Lewin, J. van Paradijs, E. P. J. van den Heuvel (Cambridge University Press), 1